JOURNAL OF THERMOPHYSICS AND HEAT TRANSFER
Vol. 9, No. 3, July–September 1995

Analysis of the Photodiode Boundary-Layer Transition Indicator

David W. Kuntz,* Andrew C. Wilken,† and Jeffrey L. Payne‡
Sandia National Laboratories, Albuquerque, New Mexico 87185

The photodiode transition indicator is a device that has been successfully used to determine the onset of boundary-layer transition on numerous hypersonic flight vehicles. The exact source of the electromagnetic radiation detected by the photodiode at transition was not understood. During some flight tests early saturation of the device occurred, and the device failed to detect transition. Analyses have been performed to determine the source of the radiation producing the photodiode signal. Four proposed radiation sources were investigated: 1) radiation from the quartz window material, 2) radiation from the heat shield material bordering the quartz window, 3) radiative emissions from the gases within the boundary and shock layers, and 4) radiation from ablation products. The results of these analyses indicate that the most likely source of the radiation is blackbody emission from the heat shield material bordering the quartz window of the device. Good agreement between flight data and calculations based on this radiation source has been obtained. Analyses also indicate that the most probable source of the radiation causing early saturation is blackbody radiation from carbon particles that break away from the nosetip during the ablation process.

Nomenclature

A_{hsr} = area of a heatshield region
A_{qd} = area of a quartz disk
$E_{B,\lambda}$ = spectral blackbody emissive power
$F_{\text{hsr-pd}}$ = view factor from a heatshield region to the photodiode
$F_{\text{qd-pd}}$ = view factor from a quartz disk to the photodiode
$I_{T,\text{hsr}}$ = photodiode terminal current resulting from the emissions of a heat shield region
$I_{T,\text{qd}}$ = photodiode terminal current resulting from the emissions of a single quartz disk
K = maximum theoretical transmittance
L = flight vehicle length
M_∞ = freestream Mach number
n = index of refraction
R = single surface reflection loss
$R_{\text{pd},\lambda}$ = photodiode spectral response
r^* = distance from vehicle surface, divided by the distance from the surface to the shock wave
T_p = carbon particle temperature
t_{qd} = thickness of a quartz disk
x = axial position on the flight vehicle
y = distance from the vehicle surface
y^+ = dimensionless distance from the wall, $y^+ = y\sqrt{\tau\rho}/\mu$
$\alpha_{\lambda,T}$ = spectral absorption coefficient
ε = total emissivity
$\varepsilon_{\lambda,T}$ = spectral emissivity
λ = wavelength
μ = dynamic viscosity
ρ = density
τ = wall shear stress
$\tau_{\lambda,T}$ = spectral transmissivity

Presented as Paper 94-0454 at the AIAA 32nd Aerospace Sciences Meeting and Exhibit, Reno, NV, Jan. 10–13, 1994; received June 24, 1994; revision received Nov. 8, 1994; accepted for publication Dec. 7, 1994.

*Senior Member of Technical Staff, Thermophysics Department. Associate Fellow AIAA.
†Distinguished Member of Technical Staff, Hypersonic Development Department.
‡Senior Member of Technical Staff, Aerosciences and Fluid Dynamics Department. Member AIAA.

Introduction

BOUNDARY-LAYER transition, the change of the fundamental nature of a boundary layer from a laminar to a turbulent state, is one of the most critical phenomenon in high-speed flight. As a boundary layer changes from laminar to turbulent, the drag on the vehicle increases significantly, and the surface heating rises by as much as a factor of 10. The successful operation of high-speed flight vehicles may depend on the ability to sense the boundary-layer state and adjust the flight characteristics of the vehicle to avoid turbulent boundary-layer flow. The photodiode transition indicator is a device that was developed at Sandia National Laboratories for the purpose of determining the local condition of the boundary layer on a hypersonic flight vehicle.[1] The device receives an optical signal through a quartz window in the vehicle surface and senses an increase in light intensity that is directly indicative of turbulent flow. Flight tests have shown that, at transition, the photodiode produces a significant step increase in signal strength. However, the specific cause of this increased optical signal was not known. In recent flight tests, several of these devices have saturated prior to boundary-layer transition, and thus failed to provide useful data.

Analyses have been conducted to determine the exact cause of the photodiode signal, and to develop a technique for predicting the diode signal strength for given flight conditions. The results of these analyses are reported in this article.

Photodiode Transition Indicator

A diagram of the photodiode transition indicator is shown in Fig. 1. As illustrated in this figure, a conical quartz window is mounted flush with the surface of the heatshield and is held in place by a thin layer of epoxy. A silicon or gallium arsenide photodiode is mounted beneath the window such that electromagnetic radiation emitted by external sources, the quartz window material, or the heat shield material surface bordering the window material, is incident on the photodiode surface. The leads from the photodiode are connected to a load resistor, and the voltage across this resistor forms the signal used to determine boundary-layer transition.

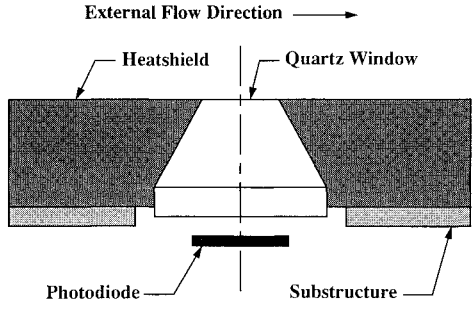

Fig. 1 Photodiode transition indicator.

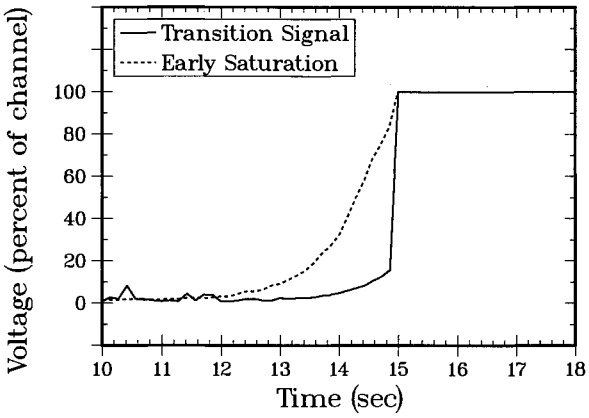

Fig. 2 Photodiode signals showing boundary-layer transition and early saturation.

The photodiodes discussed in this article are operated in what is known as the linear response mode, such that the load resistance is relatively small, and subsequently, the photodiode voltage is small. This mode of operation results in the current through the load resistor being linearly proportional to the photon flux on the photodiode surface.

For a properly functioning photodiode transition indicator, the load voltage rises extremely rapidly at boundary-layer transition. This is illustrated with the solid curve in Fig. 2, which shows the load voltage, plotted in percent of the telemetry channel full scale, as a function of time measured from an arbitrary reference. The near instantaneous rise in voltage as boundary-layer transition passes over the quartz window is visible at a time of approximately 15 s. The situation in which the load voltage saturates the telemetry channel prior to transition is illustrated as the dashed curve in Fig. 2, in which the voltage rises smoothly to the full-scale limit, without the characteristic rapid rise associated with transition. In the case of the data presented as the dashed curve in Fig. 2, the fact that transition occurred after the photodiode saturated was confirmed with thermocouple data.

The data presented in Fig. 2 was obtained from photodiodes mounted on a ballistic re-entry vehicle flying a nominal Intercontinental Ballistic Missile (ICBM) trajectory. The vehicle was equipped with a carbon–carbon nosetip and a carbon–phenolic heat shield. The conical heat shield, in which the photodiodes were mounted, had a cone half-angle of approximately 6 deg. The photodiode that produced the transition signal presented in Fig. 2 was located at an axial position near the center of the vehicle ($x/L = 0.63$), and the photodiode that produced the early saturation signal presented in Fig. 2 was located at an axial position significantly farther forward on the vehicle ($x/L = 0.31$). The uncertainty in the photodiode voltage measurements is 0.2%. As part of the flight experiment, this vehicle experienced a rapid deceleration near the end of the flight, which resulted in the signal from the center photodiode returning to a near zero value. This signal dropoff will be presented later in this article with analysis results. Unfortunately, the forward photodiode failed during the deceleration process, and thus produced no data during the signal dropoff.

In order to specify the circuit parameters and telemetry channel limits required to prevent diode saturation prior to boundary-layer transition, it is necessary to model the characteristics of the photodiode transition indicator. This model development effort depends upon a clear understanding of the source of the electromagnetic radiation causing the signal. In order to determine the source of the radiation, and to develop a model of the photodiode transition indicator, detailed analyses of the device were performed. Each of these analyses was directed towards determining the likelihood that a proposed radiation source was responsible for the photodiode transition signal. Four proposed radiation sources were investigated: 1) radiation from the quartz window material, 2) radiation from the heat shield material bordering the quartz window, 3) radiative emissions from the gases within the boundary and shock layers, and 4) radiation from ablation products. The results of these analyses are summarized in the sections that follow.

Radiating Quartz Analysis

The source of the photodiode transition signal originally proposed in Ref. 1 involves radiation from the quartz window material. The temperature of the surface of the quartz window rises rapidly at boundary-layer transition due to the near instantaneous rise in heating rate. It was proposed that the associated rapid rise in temperature resulted in the quartz material emitting in a portion of the electromagnetic spectrum that is within the spectral response of the photodiode. In order to determine whether or not the quartz was the source of the radiation sensed by the photodiode at transition, a detailed analysis of the quartz window material and the resulting photodiode response was performed. The analysis was performed using the geometry and flight conditions for the center photodiode that produced the transition signal shown in Fig. 2.

Aerodynamic Heating Calculations

The aerodynamic heating on the quartz window and surrounding heat shield material was calculated with the GE2IT[2]–SANDIAC[3]–HIBLARG[4] family of computer programs for the high-velocity portion of the flight ($M_\infty > 2$), and with the LOVEL[5] computer program for the low-velocity portion of the flight ($M_\infty \leq 2$). GE2IT solves for the inviscid flowfield in the vicinity of the spherical nosetip, SANDIAC solves for the inviscid flowfield over the conical portion of the body, and HIBLARG solves the integral boundary-layer equations over the surface in order to determine the cold-wall heating rates and boundary-layer edge conditions for both laminar and turbulent flow. LOVEL uses analytical and empirical relations to determine cold-wall heating rates and boundary-layer edge conditions on simple geometries at relatively low Mach numbers. The boundary-layer transition time was set equal to that obtained on the flight vehicle at the photodiode locations. The GE2IT–SANDIAC–HIBLARG codes predicted an increase in cold-wall heating rate of a factor of 6.2 at boundary-layer transition. This increase was assumed to occur over a time span of 0.1 s.

Material Thermal Response

The conical shape of the quartz window and the need to predict the quartz temperature distribution as accurately as possible resulted in the need to perform a two-dimensional axisymmetric material response analysis of the quartz and surrounding heat shield material. For this analysis, the FCV[6] computer program, currently under development at Sandia National Laboratories, was used. This code uses a moving-mesh algorithm to model ablating two-dimensional geometries utilizing either a heat of formation and melt temperature

ablation model or a specified surface recession rate and surface temperature boundary condition.

At the time this analysis was performed, FCV was not capable of solving a problem with two different ablating materials. Thus, the specified surface recession rate and surface temperature boundary condition was used, and the surface recession rates and the surface temperatures for the quartz and the heat shield material were determined using the one-dimensional ablation–thermal response program SODDIT.[7] Within this program, the heat of formation and melt temperature ablation model was used to determine the necessary boundary-layer conditions for the quartz and heat shield materials for the FCV calculations.

Photodiode Response Model

The radiative emission of the quartz was modeled by dividing the window into a series of thin layers that were treated as disks radiating to the photodiode surface. Each thin layer of quartz was assumed to be at a uniform temperature that was calculated from the radial temperature distribution obtained from the FCV solution with an area-averaging technique.

The current produced by the photodiode at each time step, as a result of the radiation emitted by a single quartz disk, can be determined from the relation:

$$I_{T,\mathrm{qd}} = \int (A_{\mathrm{qd}} F_{\mathrm{qd\text{-}pd}} \varepsilon_{\lambda,T} E_{B,\lambda} \tau_{\lambda,T} R_{\mathrm{pd},\lambda})\, \mathrm{d}\lambda$$

In this equation, $F_{\mathrm{qd\text{-}pd}}$, the view factor from the quartz disk to the photodiode, was obtained from Ref. 8.

The spectral emissivity of the quartz disk is obtained from the relation:

$$\varepsilon_{\lambda,T} = 1 - \exp(-\alpha_{\lambda,T} t_{\mathrm{qd}})$$

The absorption coefficient $\alpha_{\lambda,T}$ is both a function of wavelength and temperature. High-temperature absorption coefficient data for Dynasil, the quartz material flown on the re-entry vehicle, was not available, and thus data for a similar material, General Electric Type 151, obtained from Ref. 9, was used. Linear extrapolation in temperature was necessary to estimate absorption coefficients near the quartz melt temperature.

The total transmissivity of the quartz between the radiating disk and the photodiode $\tau_{\lambda,T}$ was obtained from the relation:

$$\tau_{\lambda,T} = K \prod [\exp(-\alpha_{\lambda,T} t_{\mathrm{qd}})]$$

Here, the product is taken over all the quartz disks between the disk of interest and the backface of the window. The quantity K, the maximum theoretical transmittance, is obtained from the relation:

$$K = (1 - R)$$

where R is the single surface reflection loss obtained from the index of refraction n, from the relation:

$$R = [(n - 1)/(n + 1)]^2$$

The spectral response curve of the silicon photodiode $R_{\mathrm{pd},\lambda}$ was obtained experimentally at Sandia National Laboratories, and is presented in Fig. 3. The photodiode has a sensitivity range from wavelengths of approximately 350 to 1200 nm. Thus, in this analysis, integrations over wavelength were performed between these limits.

The total current emitted by the photodiode at a given time is determined by summing the contributions from each quartz disk, thus including the effects of radiation emitted from within the entire quartz window. The load voltage is then determined by taking the product of the total current and the resistance of the load resistor. As mentioned above, the photodiodes are operated in the linear mode, such that the current is not a function of the size of the load resistor over the range of interest.

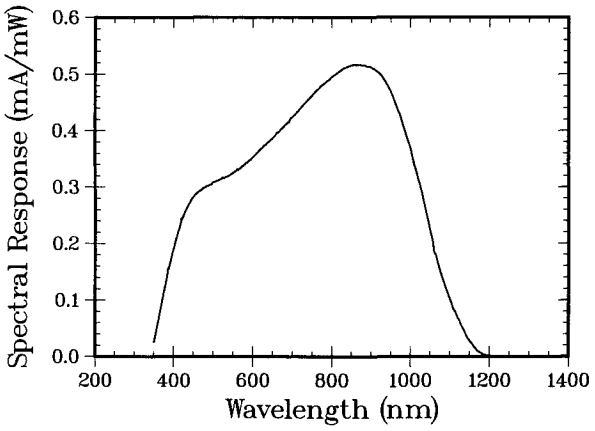

Fig. 3 Photodiode spectral response.

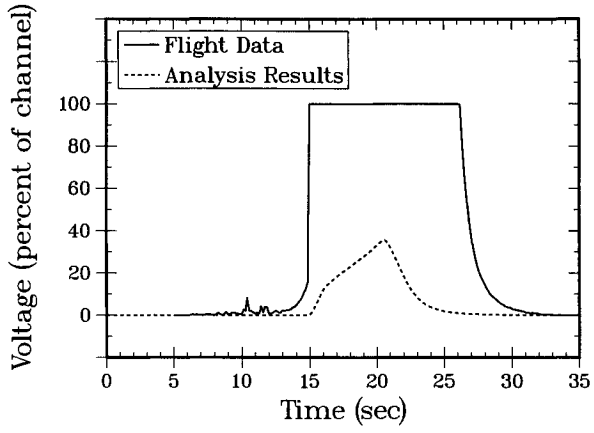

Fig. 4 Radiating quartz analysis results for the center photodiode.

Radiating Quartz Results

The results of the radiating quartz model analysis are compared with flight data in Fig. 4 for the center photodiode on the flight vehicle. As mentioned previously, this re-entry vehicle experienced a rapid deceleration after boundary-layer transition. The effects of this deceleration can be seen in the flight data, where the photodiode signal returns to its original level between a time of 25–30 s.

The results shown in Fig. 4 indicate that, although the quartz does emit at a level that can be detected by the photodiode, this radiation within the spectral response of the photodiode is not sufficient to generate the signal observed at boundary-layer transition. This result is primarily due to the relatively low emissivity of the quartz material in the wavelength band that is visible to the photodiode. Thus, an additional source of radiation must be present to generate the measured signal.

Radiating Heat Shield Material Analysis

A second proposed source of the electromagnetic radiation detected by the photodiode involves the heat shield material surrounding the photodiode assembly. The relatively low thermal conductivity of the heat shield results in its surface temperature rising extremely rapidly at boundary-layer transition to an ablation temperature of approximately 3330 K. Although the quartz window is surrounded by a thin layer of epoxy, the epoxy fails at a temperature of approximately 560 K, and the heat shield material, at high temperatures, expands to fill any gap between the heat shield and quartz left by the

failed epoxy. The relatively high emissivity of the heat shield material, and its high ablation temperature, indicate that radiation from the heat shield through the edges of the quartz window to the photodiode is a likely source of the sudden change in photodiode signal observed at boundary-layer transition.

Aerodynamic Heating Calculations

The aerodynamic heating calculations used in this analysis are the same as those used in the radiating quartz analysis. Since cold-wall heating rates are calculated independently of material properties and surface temperatures, the same results apply to the quartz window material and the surrounding heat shield material.

Material Thermal Response

The two-dimensional material response computed with the SODDIT and FCV codes for the radiating quartz analysis was also used in the present analysis. The results of these computations provided the temperature history of the epoxy/heat shield material layer bordering the quartz window necessary for this analysis.

Photodiode Response Model

The photodiode response model for the radiating heat shield material analysis is similar to that used in the radiating quartz analysis. The conical/cylindrical window edge surface was divided into thin regions. These surfaces were assumed to be at a uniform temperature, equal to the temperature at the junction of the window and surrounding material at the depth of the region's center. Radiation from each of these surfaces was transmitted through the quartz window to the photodiode surface.

The current produced by the photodiode at each time step as a result of the radiation emitted by a single region of the surrounding heat shield can be determined from a relation similar to that used in the radiating quartz analysis:

$$I_{T,\mathrm{hsr}} = \int (A_{\mathrm{hsr}} F_{\mathrm{hsr\text{-}pd}} \varepsilon E_{B,\lambda} \tau_{\lambda,T} R_{\mathrm{pd},\lambda})\, \mathrm{d}\lambda$$

The total transmissivity of the quartz between the radiating surface and the photodiode $\tau_{\lambda,T}$, was obtained from a similar relation as that used in the radiating quartz analysis:

$$\tau_{\lambda,T} = K \prod [\exp(-\alpha_{\lambda,T} t_{\mathrm{qd}})]$$

Here, the product is taken over all the quartz disks between the radiating surface and the backface of the window. The quantity K is the maximum theoretical transmittance and is obtained from the relation:

$$K = (1 - R)^2$$

This equation differs from that used in the radiating quartz analysis in that the quantity $(1 - R)$ is squared to account for both the reflective losses at the quartz surface next to the radiating surface and the reflective losses at the base of the window.

Similar to the radiating quartz analysis, the total current emitted by the photodiode at a given time due to radiation from the heat shield/epoxy surface is determined by summing the contributions from each conical/cylindrical region, thus including the effects of radiation from the complete window boundary. The load voltage is then determined, as in the radiating quartz analysis, by taking the product of the total current and the resistance.

Radiating Heat Shield Material Results

The results of the radiating heat shield analysis are compared with flight data obtained from the center and forward photodiodes in Fig. 5. The model predicted the nearly instantaneous rise in the center photodiode signal at boundary-layer transition, and predicted reasonably well the signal rise prior to transition and the signal dropoff during the deceleration portion of the flight for this photodiode. Considering the accuracy with which aerodynamic heating and material response can be predicted, this agreement is thought to be quite good, indicating that radiation from the heat shield material surrounding the quartz window is very likely the primary source of the photodiode signal.

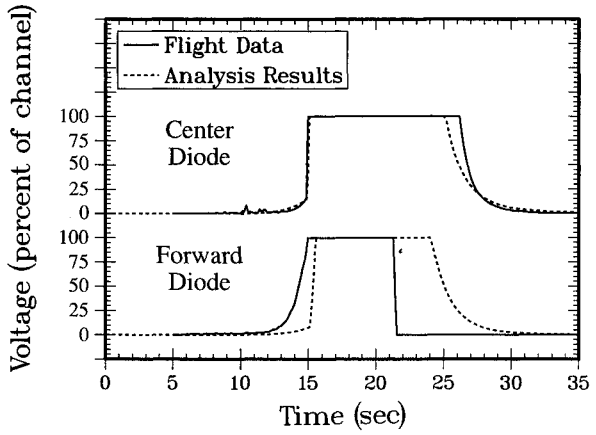

Fig. 5 Radiating heat shield analysis results for the center and forward photodiodes.

The results of the radiating heat shield analysis were compared with the forward photodiode flight data and are presented as the lower set of curves in Fig. 5. The sudden drop in the flight data between 21–22 s is due to the failure of the photodiode circuitry. The analysis predicted that the photodiode that saturated prior to transition should have produced a good transition indication, characterized by a low signal prior to transition followed by a rapid rise in signal at the time of transition, similar to that seen in the center photodiode flight data. Thus, it is apparent that the source of the signal that causes early photodiode saturation does not come solely from blackbody radiation from the heat shield material, and an additional source must be responsible.

Radiating Boundary-Layer Analysis

A third proposed source of the photodiode signal is radiative emissions from the gases within the boundary and shock layers above the surface of the quartz window. In order to determine the strength of these emissions, and the likelihood that they are responsible for part or all of either the photodiode signal increase seen at boundary-layer transition or the early saturation of photodiodes in some situations, analyses were performed for the center and forward photodiodes whose signals were initially presented in Fig. 2. The flowfield solution, including chemistry, was computed with the INCA code.[10] The radiation from the boundary layer was computed with the GENRAD code, which uses Park's NEQAIR[11-13] subroutine. The response of the photodiode to the calculated spectrum was determined with a photodiode response model similar to those described above. Due to the computational expense of the INCA solution, only two solutions were obtained, a laminar solution and a turbulent solution, for conditions which existed at a reference time of 15 s. This time corresponds to the time of boundary-layer transition for the center photodiode shown in Fig. 2, and the time of saturation for the forward photodiode also shown in Fig. 2.

Flowfield Solution

The flowfield in the vicinity of the re-entry vehicle was calculated with the INCA code. The INCA code solves the Navier–Stokes equations that account for multichemical spe-

cies and energy modes with thermochemical nonequilibrium. An LU-SGS[14,15] (lower-upper symmetric Gauss–Seidel) implicit finite volume method was used to solve the conservative form of the governing equations. The reaction rates are defined by the law of mass action and, for this simulation, Park's[16] two-temperature model provided the coefficients for the Arrhenius expressions. In this model, the vibrational, electron, and electronic temperatures are assumed to be equal, and the translational and rotational temperatures are assumed to be equal. The turbulent case was addressed using the Baldwin–Lomax model.[17]

The flowfield solutions around the axisymmetric hypersonic flight vehicle discussed above were obtained for both laminar and turbulent flow for identical freestream conditions. The flow domain was divided into three zones: 1) the nosetip region (125 by 85 grid points), 2) the forward photodiode region (92 by 85 grid points), and 3) the center photodiode region (20 by 85 grid points). In order to ensure reasonable accuracy in predicting the temperature profile near the wall, 15–20 vertical grid points were maintained in the thermal layer along the body. This computational grid resulted in y^+ values of the grid points nearest the wall at the center photodiode location of 0.08 and 0.17 for the laminar and turbulent solutions, respectively, and at the forward photodiode location of 0.05 and 0.10 for the laminar and turbulent solutions, respectively. These values are quite small, indicating that the grid was sufficiently fine to capture the flowfield details near the wall.

The flight conditions of the hypersonic flight vehicle were in a region where slight ionization occurs. Since it was possible that a small amount of ions could be the source of the radiative emissions, the 11-species, 31-reaction Park model[16] was used. The modeling of turbulent reacting flowfields is a difficult task and the physics models are not completely adequate for reacting gas mixtures in the Navier–Stokes code employed. There are some weaknesses in the modeling, and the turbulent solution should be viewed accordingly.

Figures 6 and 7 show the calculated molecular and ion mass fraction and the translational/rotational temperature distributions for the laminar case. Significant dissociation of nitrogen and oxygen occurs only in the highest temperature regions of the boundary layer, with ion mass fractions being low in the entire flowfield. The differences in the calculated temperatures between the laminar and turbulent flowfields result in only minor differences in the calculated mass fractions, primarily near the wall, where the peak temperature lies closer to the wall in the turbulent flowfield compared to the laminar flowfield.

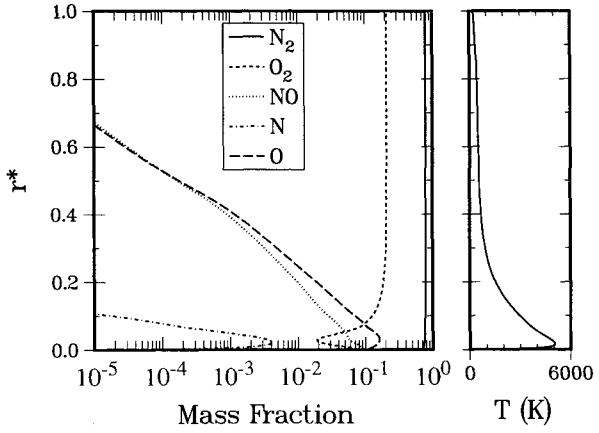

Fig. 6 Calculated laminar mass fractions and translational/rotational temperature.

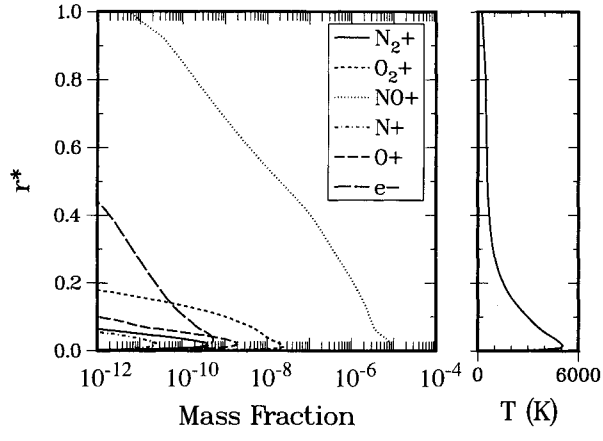

Fig. 7 Calculated laminar ion mass fractions and translational/rotational temperature.

Boundary-Layer Emissions

The results obtained from the INCA solutions were used as inputs to the GENRAD code to determine the spectra of the line emissions from the high-temperature gases within the boundary and shock layers. Initial calculations indicated that the gases could be treated as optically thin, and thus the spectra were calculated with bin widths of 5 Å. Figure 8 presents the calculated spectra for the laminar case. It can be seen in this figure that the majority of the spectral intensity is in the uv range, with the intensity falling by approximately an order of magnitude from a wavelength of 200 nm, the shortest wavelength calculated, to a wavelength of 350 nm, the lower cutoff wavelength of the photodiode response curve (Fig. 3). The calculated laminar and turbulent spectra are very similar, with only subtle differences resulting from the differences in the calculated temperatures and chemical compositions for each solution.

Photodiode Response

The photodiode response model for the spectral gas emissions is similar to that used in the radiating quartz analysis. The product of the laminar or turbulent spectrum and the photodiode spectral response is integrated over wavelength, taking into account both the absorption of the quartz window as a function of wavelength and temperature, and the geometry of the photodiode–window assembly.

The results of these calculations indicate that the photodiode response to the radiation emitted from the gases within the boundary and shock layers is less than 0.1% of the photodiode saturation level for laminar and turbulent solutions for both photodiodes. This is a result of the low spectral emissions within the wavelength band detected by the photodiode. Thus, it is apparent that emissions from the high-temperature gases cannot be responsible for either the signal

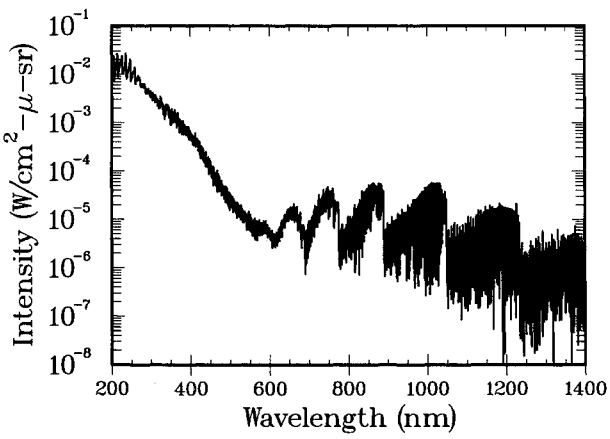

Fig. 8 Calculated laminar air spectrum.

change seen at boundary-layer transition, or the early saturation of photodiode signals, as shown in Fig. 2.

Radiating Ablation Products Analysis

A fourth proposed source of the photodiode signal is radiative emission from the ablation products produced by the nosetip and heat shield upstream of the photodiode window. These ablation products can be in the form of carbon compounds produced by chemical reactions between the carbon and the high-temperature gases in the boundary layer, or in the form of solid carbon particles that have broken away from the nosetip or heat shield and are entrained within the gases near the surface of the vehicle. Chemical compounds resulting from the ablation of the phenolic within the heat shield were not considered in this analysis. Analyses were performed to investigate the possibility that radiation from ablation products results in an appreciable photodiode signal for the center and forward photodiodes whose signals were initially presented in Fig. 2. These analyses were performed for a reference time of 15 s, similar to the analysis that determined the emissions from the high-temperature gases within the shock layer.

Carbon Compound Concentrations

The carbon ablation rate from the vehicle nosetip and heat shield prior to boundary-layer transition was calculated from a combination of flight data and analysis techniques. The nosetip recession rate was measured during the flight and was used to estimate the carbon ablation rate from the spherical portion of the nosetip. The ablation rates on the conical portion of the nosetip and the heat shield were calculated using the Charring Materials Ablation code (CMA)[18] with the heating rates obtained from the GE2IT–SANDIAC–HIBLARG family of codes assuming completely laminar flow. It should be noted that the CMA code removes material as a result of chemical reactions only, and does not model mechanical removal of solid carbon due to such phenomenon as cracking and spalling. These ablation rates were then integrated over the vehicle surface area upstream of the two photodiodes in order to determine the total carbon mass flow rate over the vehicle at the photodiode stations at the analysis time. The results of these analyses indicate that, at the reference time for a laminar boundary layer, approximately 62% of the carbon removal is occurring on the spherical portion of the nosetip, 38% is occurring on the conical portion of the nosetip, and an insignificant amount is occurring on the heat shield.

In order to determine the carbon concentration in the region above the photodiode windows, it was necessary to estimate both an average velocity of the ablation products over the surface of the vehicle, and the extent into the flowfield that the carbon products have penetrated due to diffusion processes. For this analysis, the penetration depth of the carbon into the flowfield was assumed to be equal to the laminar boundary-layer thickness, which was calculated using the HIBLARG code. The mean velocity of the ablation products was set equal to the mass-averaged mean velocity within the boundary layer. Using these quantities, the mass fraction of the carbon in the laminar boundary layer in the vicinity of the center photodiode prior to transition was computed to be approximately 0.026, and the mass fraction of the carbon in the laminar boundary layer in the vicinity of the forward photodiode prior to transition was computed to be 0.060.

The carbon within the boundary layer at a photodiode station just after the transition front had passed over the window results from the laminar ablation processes occurring on the nosetip and heat shield forward of the transition front, and from the turbulent heat shield ablation occurring aft of the transition front and forward of the photodiode. To calculate the carbon concentration for this case, the GE2IT–SANDIAC–HIBLARG–CMA calculations were repeated with the boundary layer transitioning at a point approximately 15 cm upstream of the center photodiode station at a reference time of 14.8 s. The increase in heating rate associated with boundary-layer transition resulted in a significant amount of carbon introduced into the boundary layer just forward of the photodiode. Using the turbulent boundary-layer thickness at the photodiode location as the diffusion depth of the carbon, and the mass-averaged velocity within the turbulent boundary layer as the mean carbon velocity, the mass fraction of carbon within the turbulent boundary layer at the center photodiode location was computed to be approximately 0.018. In spite of the increase in the amount of carbon being entrained within the boundary layer, this value is lower than that obtained for the laminar case due to the increase in boundary-layer thickness resulting from transition, and the increase in the mass-averaged velocity within the boundary layer resulting from transition.

Carbon Compound Spectral Emissions

The equilibrium species concentrations present within the boundary layer for both the all-laminar case and the turbulent case for the center photodiode were calculated with the Aerotherm Chemical Equilibrium (ACE)[19] code using the carbon concentrations described above and the temperatures and pressures calculated with the INCA code. Equilibrium chemistry was used for this analysis both for simplicity, and due to the fact that, for the laminar case, the majority of the carbon within the boundary layer comes from the nosetip, which is a significant distance upstream of the photodiode locations, thus allowing a significant amount of time for the carbon–air chemistry to reach equilibrium prior to ablation products reaching the photodiode locations. Figures 9 and 10 show the calculated carbon concentrations and translational/

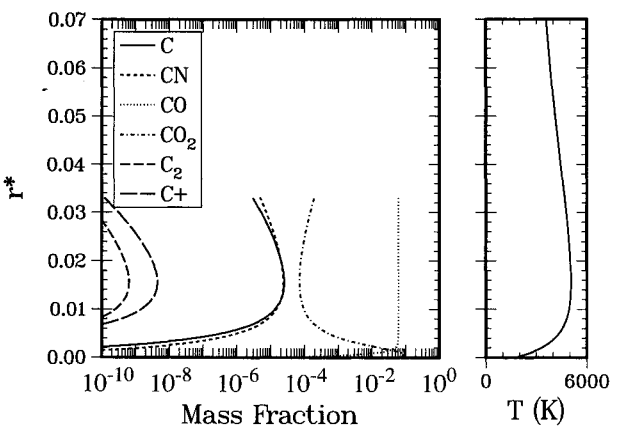

Fig. 9 Calculated laminar carbon mass fractions and translational/rotational temperature.

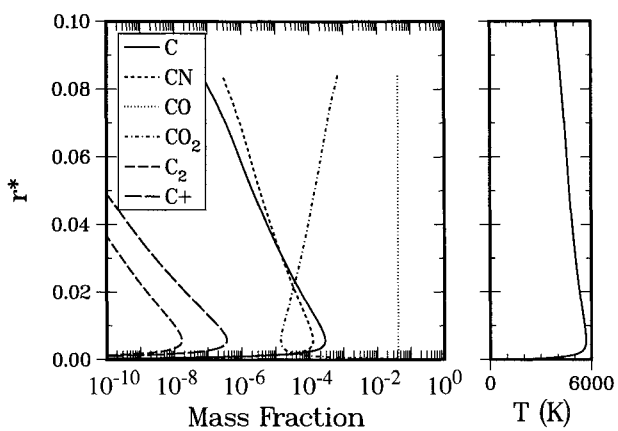

Fig. 10 Calculated turbulent carbon mass fractions and translational/rotational temperature.

rotational temperature distributions within the laminar and turbulent boundary layers, respectively, at the center photodiode location. The higher translational–rotational temperatures within the turbulent boundary layer result in significantly higher concentrations of carbon compounds and ions that extend further from the vehicle surface due to the increase in boundary-layer thickness.

The carbon concentrations within the boundary layer, along with the air species concentrations computed by the ACE program within the boundary layer, were used as input for the GENRAD code. The air species concentrations from the INCA solutions were used in the region between the boundary-layer edge and the shock wave. The spectrum obtained from the GENRAD code for the laminar solution for the center photodiode is presented in Fig. 11. The addition of carbon ablation products to the boundary layer makes a significant change to the spectrum presented in Fig. 8, with several groups of strong lines added near a wavelength of 400 nm. The greater concentration of carbon compounds in the turbulent case results in somewhat higher spectral intensities. However, in both cases, the mean spectral curve drops off above a wavelength of 400 nm, similar to what was observed in the spectra without carbon compounds present.

The photodiode response model for the carbon–air spectral emissions is identical to that used in the high-temperature air spectral analysis. The product of the spectral laminar or turbulent emission and the photodiode spectral response is integrated over wavelength, taking into account both the absorption of the quartz window as a function of wavelength and temperature and the geometry of the photodiode–window assembly. The results of these calculations, similar to the results of the air spectral analysis, indicate that the photodiode response to the radiation emitted from the combination of the ablation products and gases within the boundary and shock layers is very low, less than 0.2% of the photodiode saturation level for the center photodiode laminar case, and less than 0.5% for the center photodiode turbulent case. This again is a result of the relatively low spectral emissions within the wavelength band visible to the photodiode. Thus, it is apparent that emissions from the high-temperature ablation products and gases cannot be responsible for either the signal change seen at boundary-layer transition as presented for the center photodiode, or the early saturation of photodiode signals, such as that obtained from the forward photodiode, both of which are shown in Fig. 2.

Carbon Particle Blackbody Emissions

The carbon particle analysis was performed primarily to determine if solid particles breaking away from the nosetip could result in the saturation of the forward photodiode, as shown in Fig. 2, prior to boundary-layer transition. While carbon particles breaking away from the heat shield just aft of the transition front could contribute to the photodiode signal change resulting from transition, no analysis techniques exist for evaluating this possibility. The relatively low pressures on the heat shield surface, compared to the stagnation region of the nosetip, should result in very little mechanical carbon removal. However, this point cannot be thoroughly addressed with the analysis techniques available.

A significant amount of uncertainty also exists regarding the mechanical removal of carbon from the vehicle nosetip. This uncertainty includes such factors as the relative amount of carbon that is removed as particles, the size distribution of these particles, and the temperatures of these particles. Due to the lack of information concerning the ablation of the nosetip in the actual flight environment, a parametric analysis in particle size was performed to determine the possible effects of carbon particles on photodiode signals.

An initial analysis was performed to determine if particles removed by ablation processes from the nosetip could survive the boundary-layer environment long enough to reach the photodiode locations and to determine approximate surface temperatures for these particles. For this analysis, 1-, 10-, and 100-μm-diam particles were removed from a location on the nosetip just aft of the sphere–cone tangency point. These particles were given an initial temperature equal to the calculated surface temperature at that point on the nosetip. A one-dimensional trajectory program was used to calculate the particle velocity and position over the vehicle as a function of time, using boundary-layer edge conditions obtained from the HIBLARG code as the local flow conditions. The drag coefficients for these trajectory calculations were obtained from Ref. 20 and are based on ballistic range data. The trajectory information was then used with the HANDI[21] program to determine particle heating rate information. HANDI is a correlation-based code that solves numerous types of aeroheating related problems. The heating rate information was in turn used with the CMA code to determine particle temperature and ablation rate histories.

For each size particle used in this analysis, the calculated surface recession was small, with the largest relative surface recession calculated to be 11% of the radius for the 10-μm-diam particle. Figure 12 presents the calculated particle surface temperatures as a function of location on the vehicle. In each case, the particles undergo a rapid rise in temperature due to the initially high heating rates resulting from the large difference in velocity between the particles and the boundary-layer gases. After the particles have accelerated to velocities relatively close to the boundary-layer gases, the particles begin to cool, with the smaller particles cooling the most rapidly.

The photodiode signal resulting from carbon particles removed from the nosetip of the vehicle was computed in a similar fashion as the other signal sources described above. The calculations were performed parametrically in both par-

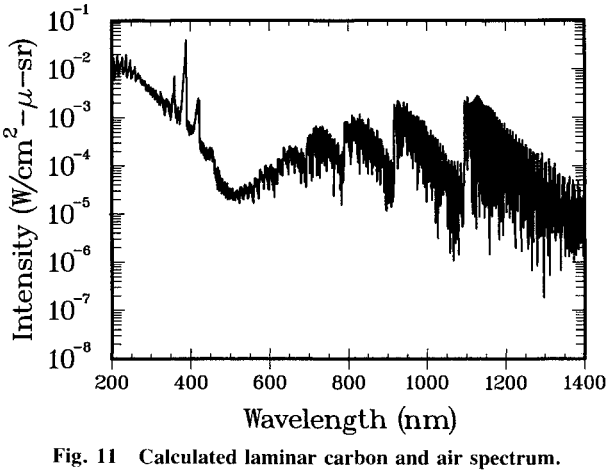

Fig. 11 Calculated laminar carbon and air spectrum.

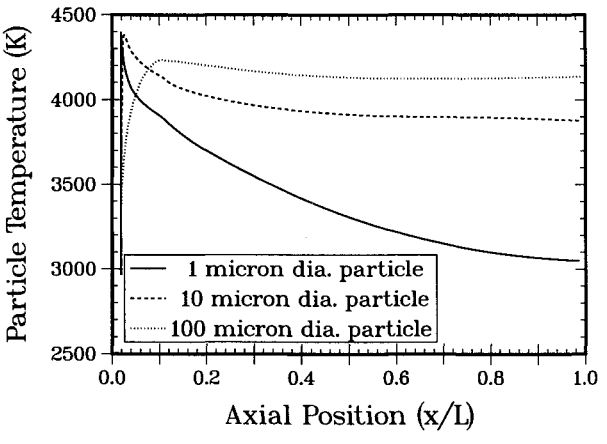

Fig. 12 Calculated particle surface temperatures.

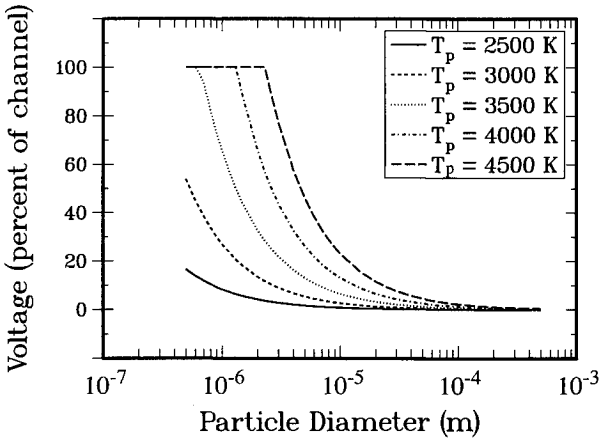

Fig. 13 Calculated photodiode signal resulting from carbon particles.

ticle size and temperature, assuming that all the mass removed from the nosetip was in particle form. Thus, the amount of carbon within the boundary layer was independent of particle size. The distribution of carbon within the boundary layer was sufficiently sparse such that the radiation from one particle toward the photodiode will not be blocked by other particles, and thus the radiation reaching the photodiode can be considered to be the superposition of the radiation from numerous particles. The particles were assumed to be spherical in shape, and the appropriate shape factor for the radiation calculation was obtained from Ref. 8. Absorption by the quartz window as a function of wavelength was accounted for in the calculation, which involved integrating the product of the blackbody radiation reaching the photodiode and the photodiode response curve over wavelength. Figure 13 presents the results of these analyses for the center photodiode.

The results of this analysis indicate that if the particles are sufficiently small, on the order of 1 μm in diameter, and have a sufficient temperature, approximately 4000 K, they could result in the saturation of a photodiode signal. These results, combined with the calculated particle temperature histories shown in Fig. 12, offer a possible explanation for the early saturation of the forward photodiode, while the center photodiode (and other photodiodes on the same vehicle) remained unsaturated until transition. Relatively small particles of carbon, removed from the nosetip due to thermal cracking and spalling, are initially aerodynamically heated to high temperatures as they accelerate within the boundary layer. The particles then cool as they move down the vehicle, causing a significantly higher signal in the photodiodes located on the forward portions of the vehicle than those located on the aft portions of the vehicle. The uncertainties in the nosetip performance and its response to the heating environment prevent a more detailed analysis of this phenomenon, but this process does explain the difference in photodiode signals on this vehicle, as well as on a similar re-entry vehicle, which also had forward-mounted photodiodes saturate early while the aft-mounted photodiodes remained unsaturated until local boundary-layer transition occurred.

Summary

Analyses of the four proposed sources of the photodiode signal have been completed. The results of these analyses indicate that the most likely source of the radiation seen at boundary-layer transition is emission from the heat shield material surrounding the quartz window. The originally proposed source of the radiation at boundary-layer transition, emission from the quartz window material, is not sufficient to produce the signal observed in flight tests. In addition, spectral radiation from both the gases within the shock layer resulting from air chemistry and carbon ablation products is insufficient to be the cause of either the photodiode signal at transition or the early saturation prior to transition. Although there is insufficient information available on the response of the nosetip material to the heating environment to perform a detailed analysis, parametric studies indicate that a likely source of the radiation that causes early photodiode saturation is blackbody radiation from carbon particles. It is proposed that these particles break away from the nosetip, are initially heated to relatively high temperatures, and then cool as they pass down the length of the vehicle. This theory explains the tendency for forward photodiodes to saturate while photodiodes further aft on the vehicle perform normally.

Acknowledgments

This work was performed at Sandia National Laboratories, which is operated for the DOE under Contract DE-AC04-94AL85000. The authors wish to thank Bennie F. Blackwell and Donald L. Potter, both of Sandia National Laboratories, for their assistance with the FCV and ACE codes, respectively. The authors also wish to thank Ellis Whiting of NASA Ames Research Center for his valuable assistance with the GENRAD code.

References

[1]Blodgett, S. R., Conrad, B. T., Shrock, K. W., Wilken, A. C., Sterk, M. W., and Chaffin, R. J., "A Novel Reentry Vehicle Instrument—The Photodiode," *ISA Transactions*, Vol. 26, No. 3, 1987, pp. 19–23.

[2]Daywitt, J., Brant, D., and Bosworth, F., "Computational Technique for Three-Dimensional Inviscid Flow Fields About Reentry Vehicles," General Electric Co., SAMSO TR-79-5, Philadelphia, PA, April 1978.

[3]Noack, R. W., and Lopez, A. R., "Inviscid Flow Field Analysis of Complex Reentry Vehicles: Volume I, Description of Numerical Methods, Volume II, User's Manual," Sandia National Labs., SAND87-0776, Albuquerque, NM, Oct.–Nov. 1988.

[4]Polansky, G. F., "Hypersonic Integral Boundary Layer Analysis of Reentry Geometries (HIBLARG) Code Description and User's Manual Version 2.0," Sandia National Labs., SAND89-0552, Albuquerque, NM, March 1990.

[5]Thornton, A. L., "LOVEL-84: A Low-Velocity Aerodynamic Heating Code for Flat Plates, Wedges, and Cones," Sandia National Labs., SAND84-0457, Albuquerque, NM, May 1984.

[6]Blackwell, B. F., and Hogan, R. E., "Numerical Solution of 2-D Axisymmetric Heat Conduction Problems Using a Finite Control Volume Technique," AIAA Paper 91-1353, June 1991.

[7]Blackwell, B. F., Douglass, R. W., and Wolf, H., "A User's Manual for the Sandia One-Dimensional Direct and Inverse Thermal (SODDIT) Code," Sandia National Labs., SAND85-2478, Albuquerque, NM, May 1987.

[8]Howell, J. R., *A Catalog of Radiation Configuration Factors*, McGraw-Hill, New York (to be published).

[9]Beder, E. C., Bass, C. D., and Shacklefore, W. L., "Transmissivity and Absorption of Fused Quartz Between 0.22 μ and 3.5 μ from Room Temperature to 1500°C," *Applied Optics*, Vol. 10, No. 10, 1971, pp. 2263–2268.

[10]"INCA: 3D Multi-Zone Navier-Stokes Flow Analysis with Finite-Rate Chemistry, User's Manual Part 1: Input Guide," Amtec Engineering, Bellevue, WA, Jan. 1992.

[11]Whiting, E. E., Arnold, J. O., and Lyle, G. C., "A Computer Program for a Line-by-Line Calculation of Spectra from Diatomic Molecules and Atoms Assuming a Voigt Line Profile," NASA TN D-5088, March 1969.

[12]Park, C., "Nonequilibrium Air Radiation (NEQAIR) Program: User's Manual," NASA TM 86707, July 1985.

[13]Moreau, S., Laux, C. O., Chapman, D. R., and MacCormack, R. W., "A More Accurate Non-Equilibrium Air Radiation Code: NEQAIR Second Generation," AIAA Paper 92-2968, July 1992.

[14]Yoon, S., and Jameson, A., "An LU-SSOR Scheme for the Euler and Navier-Stokes Equations," AIAA Paper 87-0600, Jan. 1987.

[15]Yoon, S., and Kwak, D., "Artificial Dissipation Models for Hypersonic External Flow," AIAA Paper 88-3708, July 1988.

[16]Park, C., "Assessment of Two-Temperature Kinetic Model for Ionizing Air," *Journal of Thermophysics and Heat Transfer*, Vol. 3,

No. 3, 1989, pp. 233–244.

[17]Baldwin, B. E., and Lomax, H., "Thin-Layer Approximation and Algebraic Model for Separated Turbulent Flows," AIAA Paper 78-257, Jan. 1978.

[18]Lauger, L. M., Kaestner, P. C., and Blackwell, B. F., "Operation Instructions for Charring Material Ablation Code," Sandia National Labs., SLA-73-0745, Albuquerque, NM, Aug. 1973.

[19]Powars, C. S., and Kendall, R. M., "Aerotherm Chemical Equilibrium (ACE) Computer Program," Aerotherm Corp., Mountainview, CA, May 1969.

[20]Kuntz, D. W., and Amatucci, V. A., "Drag and Heating Modifications Implemented Within the PLUTO Computer Program," Sandia National Labs., SAND92-2519, Albuquerque, NM, Jan. 1993.

[21]Potter, D. L., Memo to W. L. Hermina, "HANDI Program Options & Radiative Subroutine Enhancements," Sandia National Labs., Albuquerque, NM, April 18, 1994.